

Transition Zone Wave Propagation: Characterizing Travel-Time and Amplitude Information

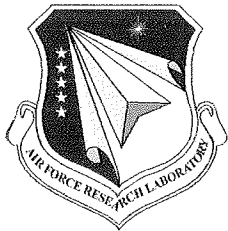
**Peter Shearer
Jesse Lawrence**

**Institute of Geophysics and Planetary Physics
Scripps Institution of Oceanography
University of California, San Diego
8800 Biological Grade
La Jolla, CA 92093-0225**

Final Report

18 January 2008

APPROVED FOR PUBLIC RELEASE; DISTRIBUTION UNLIMITED.



**AIR FORCE RESEARCH LABORATORY
Space Vehicles Directorate
29 Randolph Road
AIR FORCE MATERIEL COMMAND
Hanscom AFB, MA 01731-3010**

NOTICE AND SIGNATURE PAGE

Using Government drawings, specifications, or other data included in this document for any purpose other than Government procurement does not in any way obligate the U.S. Government. The fact that the Government formulated or supplied the drawings, specifications, or other data does not license the holder or any other person or corporation; or convey any rights or permission to manufacture, use, or sell any patented invention that may relate to them.

This report was cleared for public release and is available to the general public, including foreign nationals. Qualified requestors may obtain additional copies from the Defense Technical Information Center (DTIC) (<http://www.dtic.mil>). All others should apply to the National Technical Information Service.

AFRL-RV-HA-TR-2008-1030 HAS BEEN REVIEWED AND IS APPROVED FOR
PUBLICATION IN ACCORDANCE WITH ASSIGNED DISTRIBUTION STATEMENT.

//Signature//

ROBERT RAISTRICK
Contract Manager

//Signature//

PAUL TRACY, Acting Chief
Battlespace Surveillance Innovation Center

This report is published in the interest of scientific and technical information exchange, and its publication does not constitute the Government's approval or disapproval of its ideas or findings.

REPORT DOCUMENTATION PAGE [example]				Form Approved OMB No. 0704-0188	
Public reporting burden for this collection of information is estimated to average 1 hour per response, including the time for reviewing instructions, searching existing data sources, gathering and maintaining the data needed, and completing and reviewing this collection of information. Send comments regarding this burden estimate or any other aspect of this collection of information, including suggestions for reducing this burden to Department of Defense, Washington Headquarters Services, Directorate for Information Operations and Reports (0704-0188), 1215 Jefferson Davis Highway, Suite 1204, Arlington, VA 22202-4302. Respondents should be aware that notwithstanding any other provision of law, no person shall be subject to any penalty for failing to comply with a collection of information if it does not display a currently valid OMB control number. PLEASE DO NOT RETURN YOUR FORM TO THE ABOVE ADDRESS.					
1. REPORT DATE 23 Dec 2007		2. REPORT TYPE Final Report		3. DATES COVERED (From - To) 23 Dec 2005 to 23 Dec 2007	
4. TITLE AND SUBTITLE Transition Zone Wave Propagation: Characterizing Travel-Time and Amplitude Information				5a. CONTRACT NUMBER FA8718-06-C-0005	
				5b. GRANT NUMBER N/A	
				5c. PROGRAM ELEMENT NUMBER 62601F	
6. AUTHOR(S) P. Shearer and J. Lawrence				5d. PROJECT NUMBER 1010	
				5e. TASK NUMBER SM	
				5f. WORK UNIT NUMBER A1	
7. PERFORMING ORGANIZATION NAME(S) AND ADDRESS(ES) IGPP/SIO U.C. San Diego La Jolla, CA 92093-0225				8. PERFORMING ORGANIZATION REPORT NUMBER	
9. SPONSORING / MONITORING AGENCY NAME(S) AND ADDRESS(ES) Air Force Research Laboratory 29 Randolph Rd. Hanscom AFB, MA 01731-3010				10. SPONSOR/MONITOR'S ACRONYM(S) AFRL/RVBYE	
				11. SPONSOR/MONITOR'S REPORT NUMBER(S) AFRL-RV-HA-TR-2008-1030	
12. DISTRIBUTION / AVAILABILITY STATEMENT Approved for Public Release; Distribution Unlimited.					
13. SUPPLEMENTARY NOTES					
14. ABSTRACT We characterize transition-zone seismic wave propagation by mapping and calibrating the travel-time and amplitude behavior of <i>P</i> waves traveling through the transition zone at epicentral distances from 13 to 30 degrees and modeling the triplications resulting from the 410- and 660-km discontinuities. We have built an online database of waveforms from the IRIS FARM archive from 1990 to 2005 and process the data in order to compute source and station amplitude terms to correct for different magnitude sources and near-receiver site effects as well as errors in the instrument response functions. We use records from the full teleseismic <i>P</i> distance interval to estimate source-time-function envelopes and deconvolve them from the traces, discarding data from sources that last longer than 60 s and signals with low signal-to-noise ratios. The deconvolved traces are stacked into bins according to distance, providing an initial distance (or Earth-structure) wavefield term. Through several iterations we converge upon solutions for the event, station, and structure wavefield terms. This deconvolution technique is necessary to combine data from many different sources. We then compute both global and regional Earth-structure terms to obtain the average time-versus-distance amplitude of the wavefield, focusing on the 13 to 30 degree interval that is most sensitive to transition-zone structure. We model our data stacks using WKB synthetic seismograms and a niching genetic algorithm to explore the model space of different transition-zone velocity structures. We compare these results with long-wavelength models of 410- and 660-km discontinuity topography obtained from <i>SS</i> precursors and more detailed images beneath individual seismic stations derived from receiver functions.					
15. SUBJECT TERMS Spectral analysis, Seismic discrimination					
16. SECURITY CLASSIFICATION OF:			17. LIMITATION OF ABSTRACT	18. NUMBER OF PAGES	19a. NAME OF RESPONSIBLE PERSON Robert Raistrick
a. REPORT UNCLASSIFIED	b. ABSTRACT UNCLASSIFIED	c. THIS PAGE UNCLASSIFIED			19b. TELEPHONE NUMBER (include area code) 781-377-3726

Table of Contents

1. Summary	1
2. Technical Approach	3
3. Results and Discussion	6
4. Conclusions	15
References	16
List of Symbols, Abbreviations, and Acronyms	18

Figures

1. Discontinuities in the mantle transition zone at 410- and 660-km depths cause a pair of triplications in P - and S -wave arrivals between about 15 and 30 degrees. The ray paths (top) are color-coded, and correspond to the different branches in the travel-time curve plotted below (reduced at 10 s/degree). The AB branch consists of direct waves that bottom above the 410-km discontinuity (red solid). The BC branch reflects at 410 km (red dashed). The CD and DE branches bottom above and reflect off the 660-km discontinuity (blue solid and dashed). The EF branch bottoms in the lower mantle. This figure is adopted from Shearer (2000). 1

2. Lateral and vertical variation in seismic velocity structure (Masters et al., 2000) and mantle topography (Flanagan and Shearer, 1998) cause significant variation in the upper mantle triplications. The location of this profile is shown in the map at the center. Topography is exaggerated by 3 times. 2

3. Distance-dependent Earth-response terms for P -wave amplitude from 10 to 90 degrees. 4

4. A graphical representation of the sources of seismic signals (event, Earth response term, receiver term, and noise) that we attempt to decompose. 5

5. Examples of three different types of perturbations to transition zone structure: (a) transition zone thickness, (b) velocity contrast, and (c) interface thickness. The corresponding WKB maximum amplitudes for P waves (d-f) change as a function of distance. The models are shown as black, blue, and red lines. The data are the dashed lines. 5

6. Parameterization of the P velocity model. Each interface (410, 520, & 660) can vary in depth, thickness, and velocity contrast. 7

7. The (red) best fit model after 100 generations of an NGA simulated inversion yields a similar result to a similar parameter search based on (blue) PdP , SdS , Pds , and $Ppdp$ reflected phases (Lawrence and Shearer, 2006). 7

8. The time- and distance-dependent Earth-response function calculated from all FARM P -wave data using the spectral deconvolution method. The box outlines the region of triplicated data. Blue is positive amplitude, red is negative. Various phases are indicated as P , PP , and PcP . 9

9. The time- and distance-dependent Earth-response function calculated from all FARM P -wave data using the iterative deconvolution method. The box outlines the region of triplicated data. Blue is positive amplitude, red is negative. Various phases are indicated as P , PP , and PcP . 10

10. The amplitudes of the globally stacked Earth response function using iterative deconvolution at time zero for each distance (yellow) grossly match the average estimates from simple maximum amplitudes for *P*-waves (red). The black dots illustrate the scatter in the *P*-wave amplitudes. 11
11. This figure shows (a) the synthetic Earth-response function for the seismic velocity model found by Lawrence and Shearer (2006) (LS06), and deviations in Earth-response functions relative to LS06 as a result of (b) a deeper 660 interface, (c) a larger V_{p660} contrast, and (d) a thick 410 interface. Blue is positive, red is negative. 12
12. A comparison showing that the Earth-response function calculated from the model of Lawrence and Shearer, (2006) is very similar to the global Earth response function. These figures were calculated with decomposition using spectral division. 13
13. The Earth response term for a single event, as (a) traces, and (b) as the zero time amplitude (x's) as a function of event-to-station distance. 14
14. The relative scaling factor between the zero-time Earth-response amplitudes of a single event and the zero-time Earth-response amplitudes of the global dataset plotted versus body wave magnitude. 15

1. SUMMARY

This project studies the effects of heterogeneous transition-zone structure on seismic travel times and amplitudes. Accurate predictions of *P*- and *S*-wave travel times and amplitudes at distances between 13 and 30 degrees are hindered by the sensitivity of the multiple travel-time branches at these distances to variable structure in the mantle transition zone. Both discontinuity topography and bulk seismic velocity anomalies perturb seismic ray paths, which causes focusing and defocusing effects on wave amplitudes as well as travel-time anomalies. However, travel-time and amplitude information is critical for locating and estimating magnitudes of target events. By comparing regional variations of triplication amplitudes and travel times with predictions of 3D seismic velocity models, it is possible to obtain improvements in mantle transition-zone models, as well as in the estimated locations and magnitudes of recorded events.

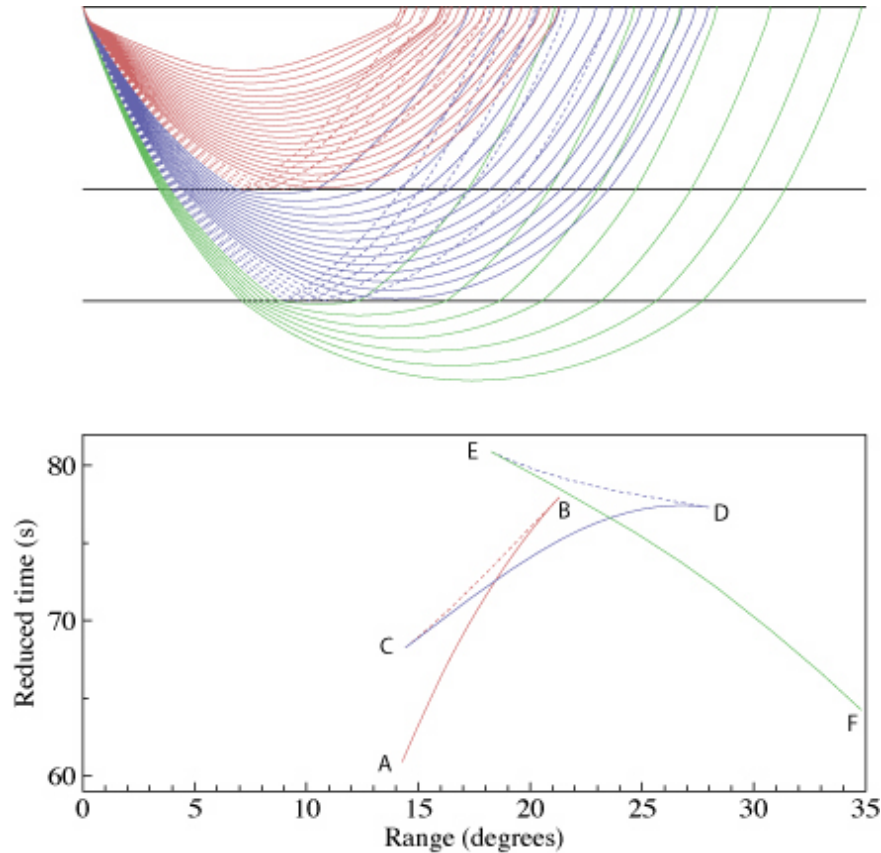


Figure 1. Discontinuities in the mantle transition zone at 410- and 660-km depths cause a pair of triplications in *P*- and *S*-wave arrivals between about 15 and 30 degrees. The ray paths (top) are color-coded, and correspond to the different branches in the travel-time curve plotted below (reduced at 10 s/degree). The AB branch consists of direct waves that bottom above the 410-km discontinuity (red solid). The BC branch reflects at 410 km (red dashed). The CD and DE branches bottom above and reflect off the 660-km discontinuity (blue solid and dashed). The EF branch bottoms in the lower mantle. This figure is adopted from Shearer (2000).

The effect of the mantle discontinuities at 410- and 660-km depth is shown in Figure 1, which depicts a series of *P*-wave ray paths between 13 and 35 degrees. Retrograde branches result from the velocity jump at each of the discontinuities, causing the familiar double triplication centered at about 20 degrees. However, the positions of these branches are very sensitive to the discontinuity depths, which typically vary by 30 km or more (e.g., Shearer, 1990, 1991, 1993; Shearer and Masters, 1992; Flanagan and Shearer, 1998a,b; Gu et al., 1998), and to the size of the velocity jumps at the discontinuities, which also exhibit considerable variation (e.g., Melbourne and Helmberger, 1998; Shearer and Flanagan, 1999; Chambers et al., 2005). In addition, there is some sensitivity to 3D velocity variations (e.g., Figure 2) in the mantle transition zone.

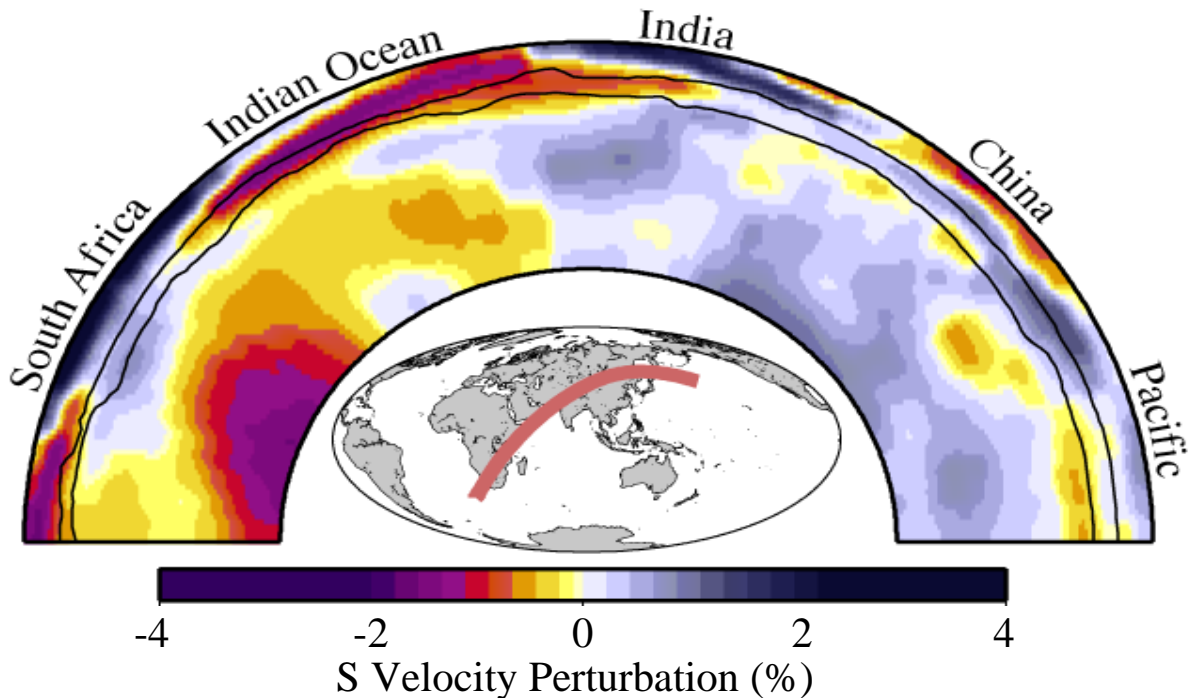


Figure 2: Lateral and vertical variation in seismic velocity structure (Masters et al., 2000) and mantle topography (Flanagan and Shearer, 1998a,b) cause significant variation in the upper mantle triplications. The location of this profile is shown in the map at the center. Topography is exaggerated by 3 times.

We compare observed *P*-wave travel times and amplitudes with predictions based on the best current models. These tests illuminate the strengths and weaknesses of these models, from which we determine if the models are sufficient to explain anomalous travel times and amplitudes at these distances (and consequently check to see how robust our current event locations and amplitude predictions are). This project compares times and amplitudes recorded at both temporary and permanent seismic stations for all triplication phases, not just the first arrivals. The triplications cause difficulties for traditional methods of source location, magnitude estimation, and inversions for 3D velocity structure. Therefore, triplication data are typically avoided for seismic tomography and

source location. However, details of the triplications can be useful for characterizing heterogeneity and calculating better source locations. With sufficient data the secondary branches can be used to model variations in discontinuity topography and seismic velocity. Once the structural properties are determined, the high sensitivity of triplication travel-time and amplitude fluctuations to source location and magnitude make triplications ideal for determining source characteristics. However, without an appropriate transition zone model, these times cannot yield accurate times or amplitudes.

The relevance of our results for nuclear test monitoring is that better models of transition-zone structure will reduce source location and magnitude uncertainties. The anomalous arrival times and amplitudes between 13 and 30 degrees currently limit the usefulness of regional phase data in calculating accurate source locations and event magnitudes. However, records from closer distances are not likely to be available in many parts of the world and small magnitude events are often not well recorded at longer distances because of the sharp drop in P and S amplitudes that occurs just beyond 30 degrees. Thus unraveling the complexities of the travel-time triplications and improving our models of the transition zone are likely to be critical for accurate monitoring of a significant number of target events.

2. TECHNICAL APPROACH

FARM Database

Our initial efforts concentrated on assembling a database of waveforms from the IRIS FARM archive, which consists of broadband data from the global seismic networks as well as portable seismic arrays deployed in PASSCAL experiments. This involves transferring the data from the IRIS DMC and converting waveforms to SAC. We then run programs for quality assurance, redundancy checks, instrument response corrections, meta-data archiving, and signal rotation to tangential and radial. The SAC files are currently stored on a RAID system, with backup for redundancy in the event of hardware failures.

We have also computed index files and signal-to-noise estimates for the P and S arrivals, which facilitates later processing and also provides a check on the timing integrity of the SAC waveforms. Our basic approach is to measure the signal-to-noise as the ratio between the maximum amplitude (peak to trough) in a time window that contains the phase of interest and a pre-event noise window of equal length. Because the raw data are broadband, we perform this operation separately for different frequency bands.

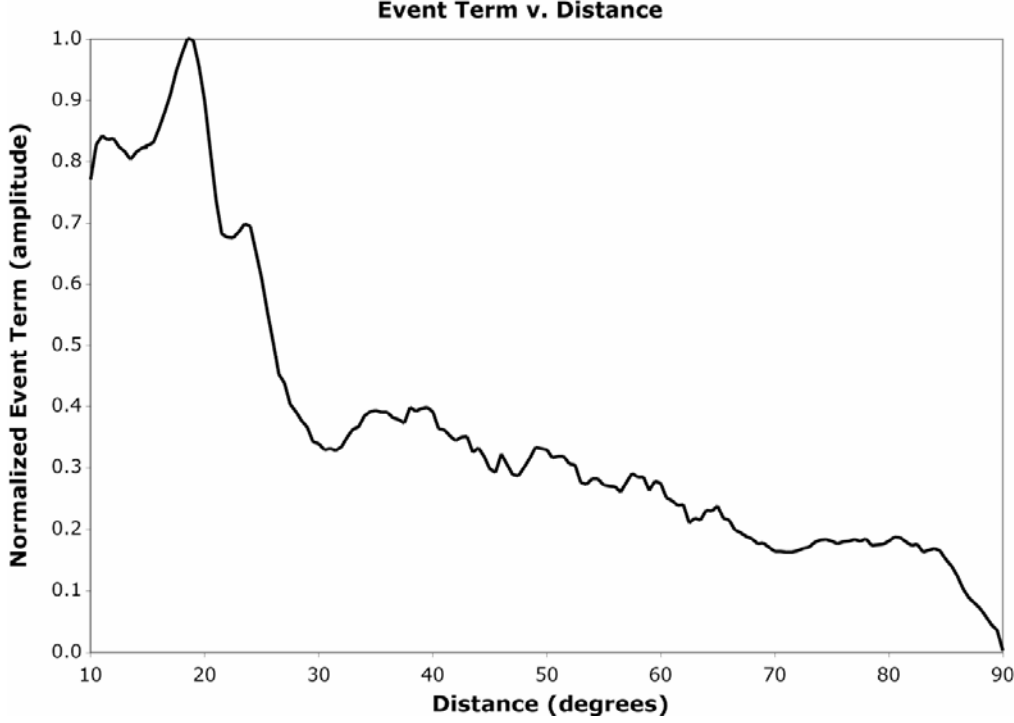


Figure 3. Distance-dependent Earth-response terms for P -wave amplitude from 10 to 90 degrees.

Amplitude Analysis

Triplicated phases are difficult to distinguish from each other, overlapping in time, and having varying amplitudes. This is further compounded by unconstrained source-time functions of the earthquake, and heterogeneous structure beneath seismic stations causing waveform variability. Here, we attempt to remove the source and station terms from all measured amplitudes for high signal-to-noise P waves, to constrain the amplitude variation that results from seismic structure. Initially we assume as in Figure 4 that the maximum peak-to-peak log amplitude (max-min), a_i , of the i^{th} P -wave is the sum of a source term, s_j , a receiver term, r_k , and an Earth response term, e_l ,

$$a_i = s_j + r_k + e_l.$$

Given N_a P -wave amplitudes, from any N_s sources, recorded at N_r sources, it is possible to solve for N_e Earth-response terms as a function of distance. The initial source term for each event is the mean of all a_i values for that event. The initial receiver terms are the means of all amplitude measurements for that receiver minus the corresponding source terms ($r_k = a_i - s_j$). The distance-dependent Earth-response term is the mean of all amplitude measurements for each distance minus the corresponding source and receiver terms ($e_l = a_i - s_j - r_k$). We can then iteratively solve for more accurate source, receiver, and Earth response terms, with

$$s_j = a_i - r_k - e_l$$

$$r_k = a_i - s_j - e_l$$

$$e_l = a_i - s_j - r_k.$$

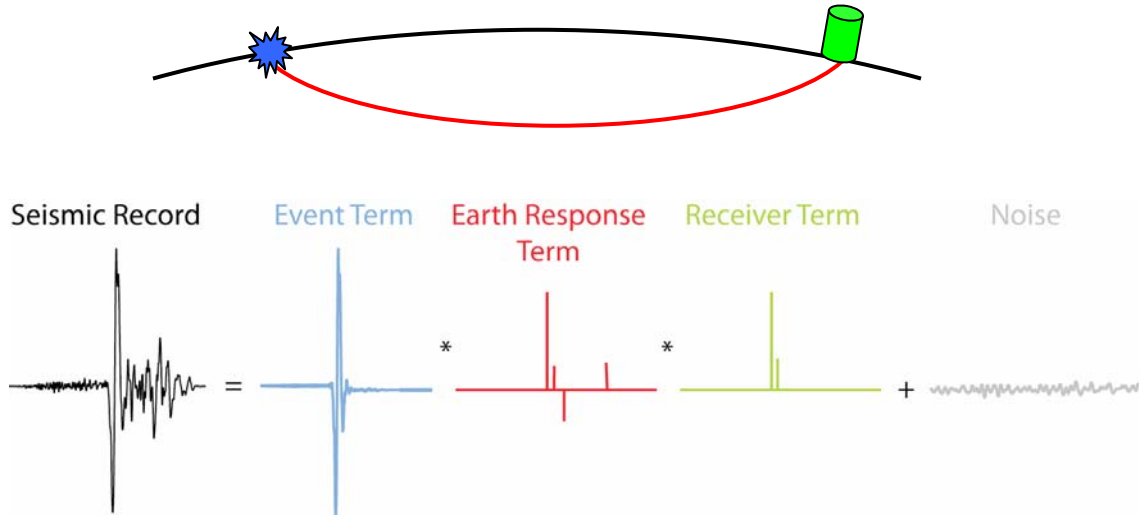


Figure 4. A graphical representation of the sources of seismic signals (event, Earth response term, receiver term, and noise) that we attempt to decompose.

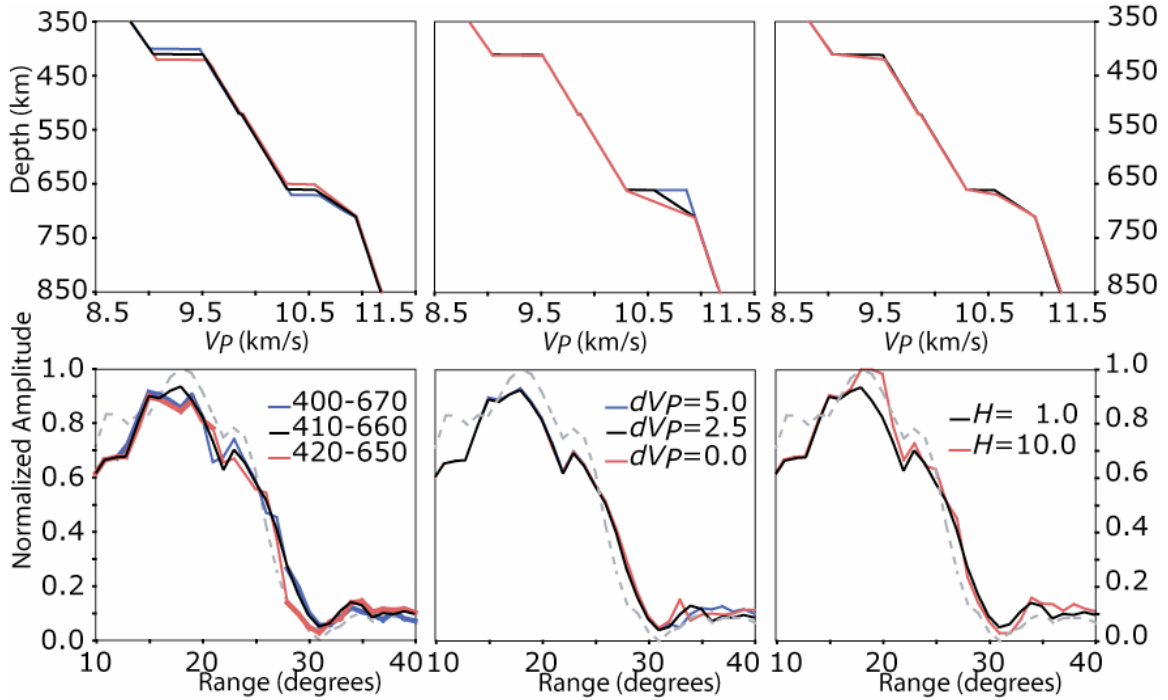


Figure 5. Examples of three different types of perturbations to transition zone structure: (a) transition zone thickness, (b) velocity contrast, and (c) interface thickness. The corresponding WKBJ maximum amplitudes for P waves (d-f) change as a function of distance. The models are shown as black, blue, and red lines. The data are the dashed lines.

When applied to all *P*-wave data in the FARM database, this method provides an estimate of amplitude as a function of distance, as shown in Figure 3. The overall amplitude versus distance behavior is very similar to that obtained by Veith and Clawson (1972) for magnitude calibration. The 13° to 33° distance range stands out as anomalous compared to the trend of decreasing amplitude with distance.

We have adapted a WKB synthetic seismogram code (Chapman, 1978) to generate suites of model predictions for comparisons to the data. Our analyses have concentrated on characterizing the globally averaged wavefield as a starting reference point for studies of regional variations. By comparing the Earth-response amplitude terms to WKB synthetic waveform amplitudes, it is possible to determine which seismic models are most probable. The amplitudes in the 13° to 33° range are sensitive to the seismic velocity structure of the transition zone. Amplitudes are highly sensitive to interface depth, sharpness, and velocity contrast for each of the discontinuities (410, 520, and 660). Figure 5 shows how amplitude can vary with small changes in seismic velocity structure. While not modeled here, the amplitudes are also strongly dependent upon attenuation structure.

3. RESULTS AND DISCUSSION

We model the data with a mass-forward modeling algorithm called the Niching Genetic Algorithm (NGA) (*Koper et al.*, 1999). The NGA uses an evolutionary paradigm to create, mutate, and breed a population of velocity structure models such that those with poor fits to the data are eliminated, and those with good fits survive to continue the search of the model space for the best solution. Using this paradigm, we find the optimal solution to the *P*-wave data (Figure 6). Using the NGA, we parameterize velocity contrast, density contrast, interface depths, and interface thickness for each interface (410, 520, and 660) as shown in Figure 6. The sub-660 gradient is defined by the interface at the bottom of the 660 and a peg depth parameter below which the *P*-wave velocity and density are equal to AK135.

The resultant model (Figure 7) is similar to the *P*-wave velocity structure found by Lawrence and Shearer (2006) using NGA waveform modeling of reflected energy from the transition zone (*PdP*, *SdS*, *Pds*, and *Ppdp*). Both models have roughly the same velocity contrasts at the 410, and 660 km discontinuities. The sub-660 gradient is identical within the resolution of each study. The estimated amplitude and depth of the 520 km discontinuity are more different, but are poorly constrained in both studies relative to the larger interfaces. In fact, the synthetic Earth-response term of the model from Lawrence and Shearer (2006) provides an equivalent fit to the observed global Earth response as the most optimal model of this study.

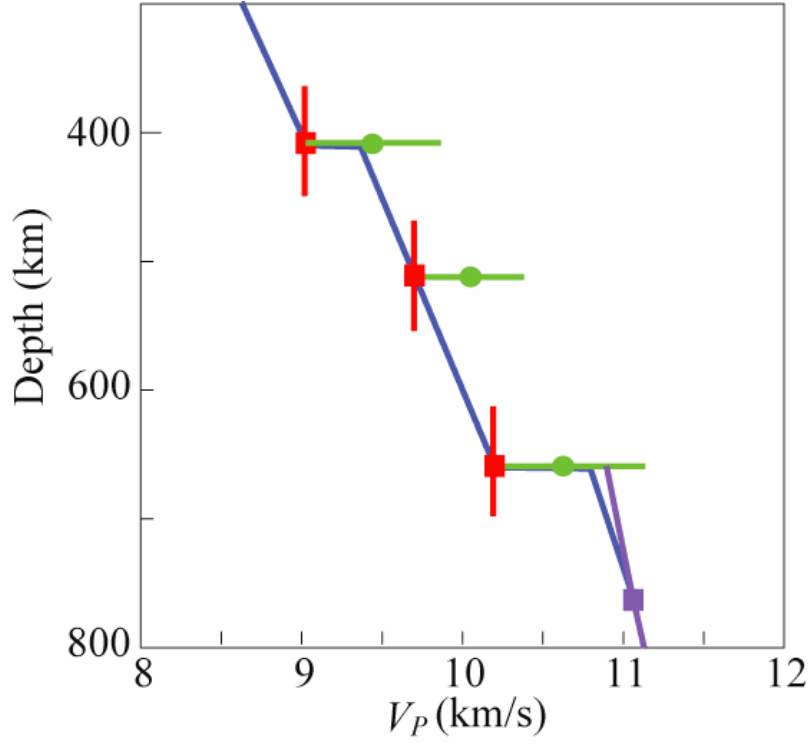


Figure 6. Parameterization of the P velocity model. Each interface (410, 520, & 660) can vary in depth, thickness, and velocity contrast.

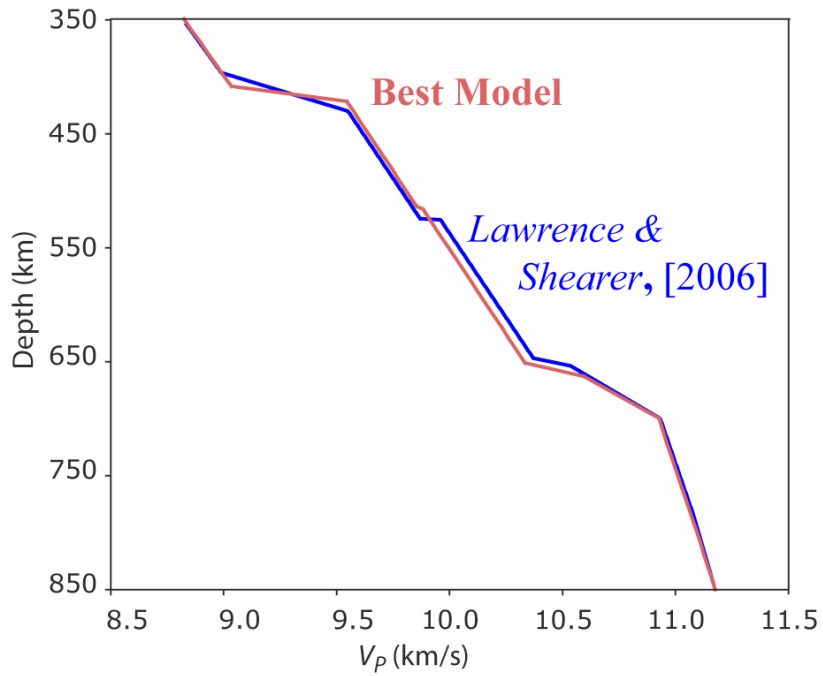


Figure 7. The (red) best fit model after 100 generations of an NGA simulated inversion yields a similar result to a similar parameter search based on (blue) PdP , SdS , Pds , and $Ppdp$ reflected phases (Lawrence and Shearer, 2006).

Wavefield Analysis

In the amplitude section, we neglected time other than to ensure that we have windowed the appropriate phase. Here, we introduce a similar analysis that iteratively solves for time-dependent source, station, and Earth-response terms. Mathematically, one can conceptualize a waveform, $a(t)$, as the convolution of the source term, $s(t)$, the receiver term, $r(t)$, and the distance-dependent Earth-response term, $e(\Delta, t)$, plus noise, $n(t)$,

$$a(t) = s(t) * r(t) * e(\Delta, t) + n(t).$$

Here, we assume that the source term, s , is a combination of the earthquake rupture and the near-source Earth response function. Furthermore, the receiver term is idealized as the convolution of the instrument response and the near-receiver Earth response.

Ideally, one could estimate the deep-Earth response by stacking waveforms with the source and receiver terms ($s(t)$ and $r(t)$) deconvolved. Unfortunately, the source and receiver terms are poorly constrained, the waveforms are not easily stackable because of dissimilarity and polarity issues, and noise is typically problematic. Therefore we develop and employ an automated stepwise stacking and deconvolution technique to boost the signal-to-noise ratio and to solve for the time-dependent source and receiver terms. We improve waveform similarity by examining the instantaneous amplitude or envelope function of the wavefield, $a_E(t)$, rather than the raw waveform. We initially estimate the source, receiver, and Earth-response functions as delta functions with amplitudes provided by the amplitude analysis above.

With preliminary estimates of s , r , and e , we can iteratively solve for each term from the envelope function,

$$\begin{aligned} s(t) &= a_E(t) *^{-1} r(t) *^{-1} e(\Delta, t) \\ r(t) &= a_E(t) *^{-1} s(t) *^{-1} e(\Delta, t) \\ e(\Delta, t) &= a_E(t) *^{-1} s(t) *^{-1} r(t) \end{aligned}$$

With this analysis, we obtain a time- and distance-dependent Earth-response term. For all data in the FARM database, the Earth-response term is shown in Figure 8 as determined with spectral deconvolution. In addition to spectral division techniques, we investigate the benefits of employing iterative deconvolution. While spectral deconvolution is computationally faster than iterative deconvolution, it is acausal, often noisy, and results depend heavily on a waterlevel. Iterative deconvolution is slower, but is causal, can solve for positive peaks only, and provides a minimum information solution. In Figures 8 and 9 we compare results of the spectral division and iterative deconvolution techniques.

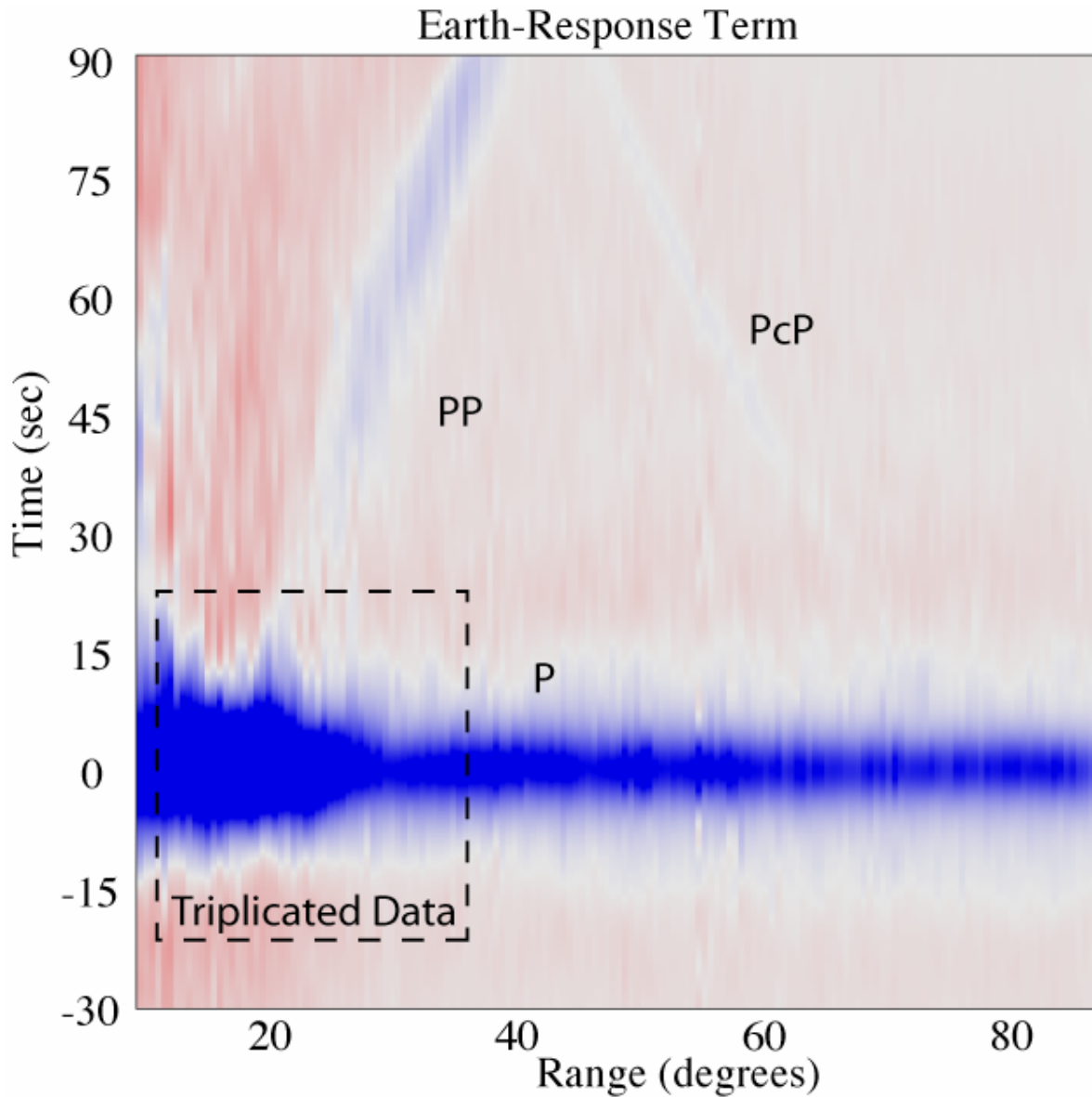


Figure 8. The time- and distance-dependent Earth-response function calculated from all FARM *P*-wave data using the spectral deconvolution method. The box outlines the region of tripllicated data. Blue is positive amplitude, red is negative. Various phases are indicated as *P*, *PP*, and *PcP*.

There appear to be significant differences between the two, but the majority of the differences are due to the longer-period smoothing necessary for the spectral division technique. Consequently some features appear to be sharper in the iterative deconvolution technique. For example, the iterative deconvolution technique provides a sharper high amplitude anomaly at 25 to 28 degrees after the initial pulse (3 to 5 seconds). This pulse is associated with the *P* branch of the 660 km discontinuity.

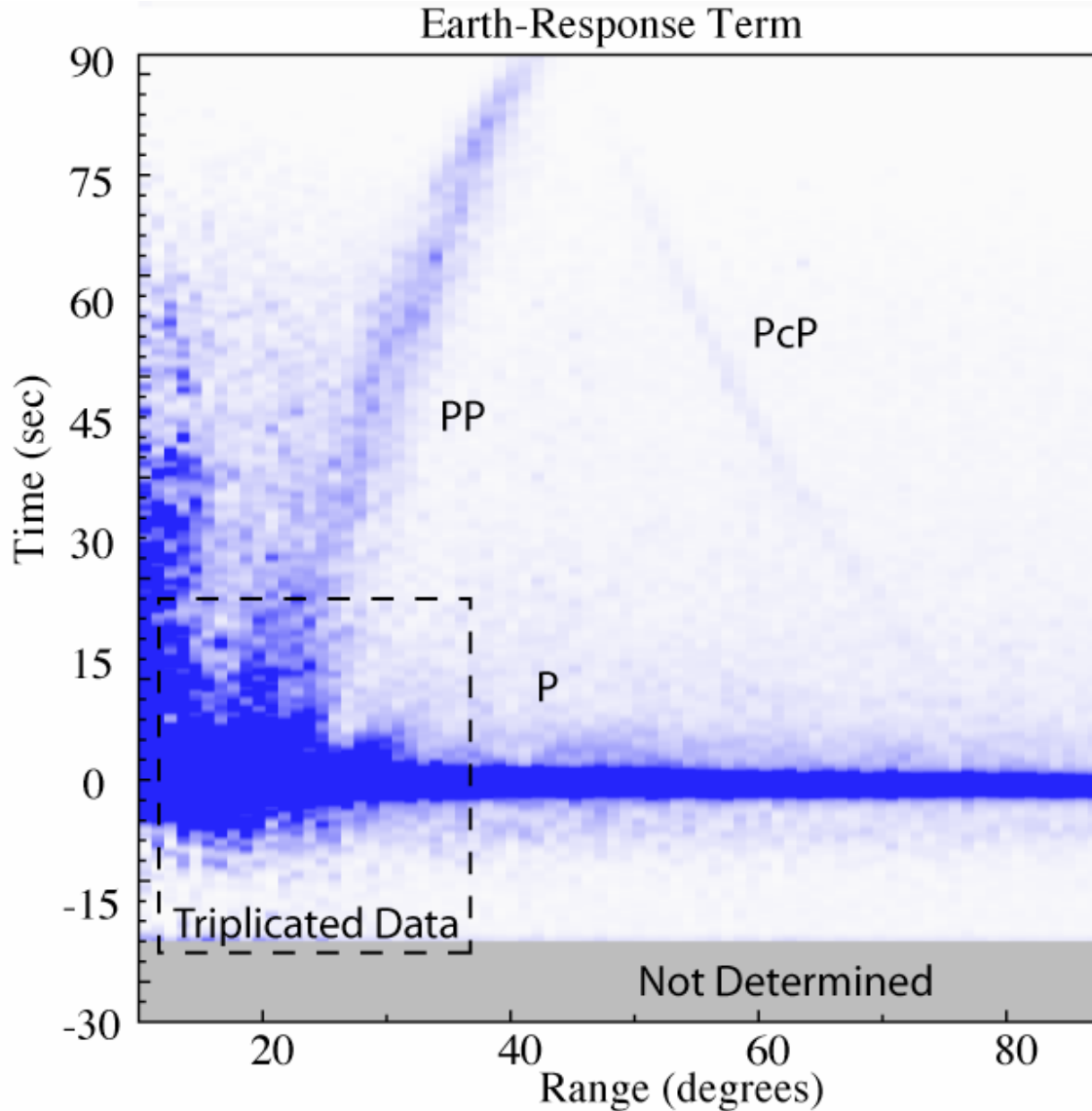


Figure 9. The time- and distance-dependent Earth-response function calculated from all FARM *P*-wave data using the iterative deconvolution method. The box outlines the region of tripllicated data. Blue is positive amplitude, red is negative. Various phases are indicated as *P*, *PP*, and *PcP*.

While the iterative deconvolution technique provides resolution at higher frequencies, the differences between the modeled synthetics for each technique shows that there is minimal improvement in resolution relative to the spectral method. While all further analyses were conducted with both the spectral division technique and the iterative deconvolution technique, we only present results from one method because of their great overall similarity.

The amplitudes of the globally stacked Earth response function using iterative deconvolution at time zero for each distance grossly match the estimates from the simpler maximum amplitude decomposition (see Figure 10). Both the raw amplitudes and the

Earth-response term amplitudes have elevated amplitudes between 10 and 30 degrees. Of particular interest, the low amplitudes observed at ~30 degrees in both amplitude distributions is continued to nearly 40 degrees in zero-time Earth-response term amplitudes. At ~40 degrees, there is a small elevated amplitude. Variations at ~35 degrees result from amplitude differences in the first arrival relative to the later arriving *P* branch from the 660 km discontinuity. The amplitudes gradually decrease from ~40 degrees to 90 degrees. Beyond 90 degrees the amplitudes decrease rapidly because of the influence of the low velocities in the outer core.

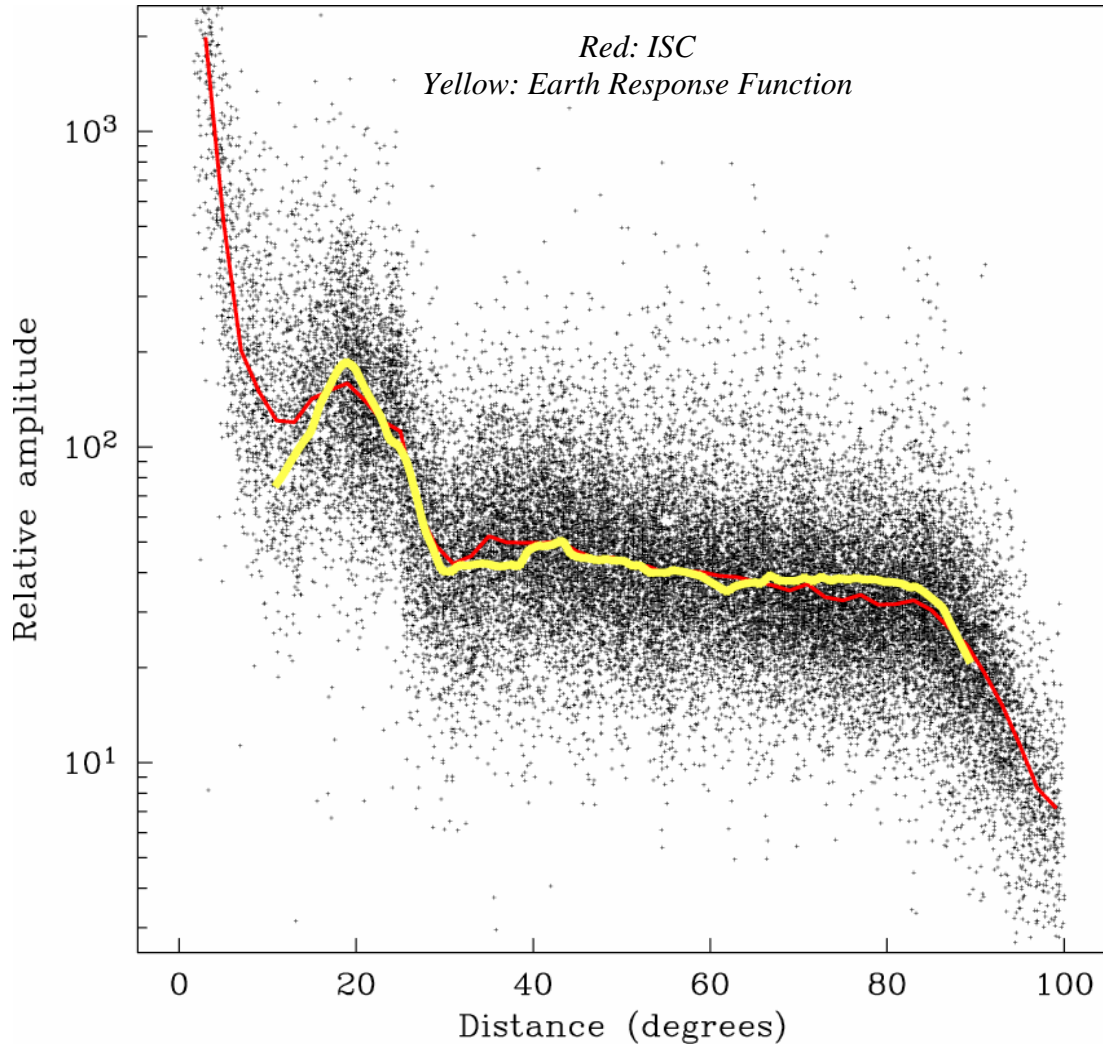


Figure 10: The amplitudes of the globally stacked Earth response function using iterative deconvolution at time zero for each distance (yellow) grossly match the average estimates from simple maximum amplitudes for *P*-waves (red). The black dots illustrate the scatter in the *P*-wave amplitudes.

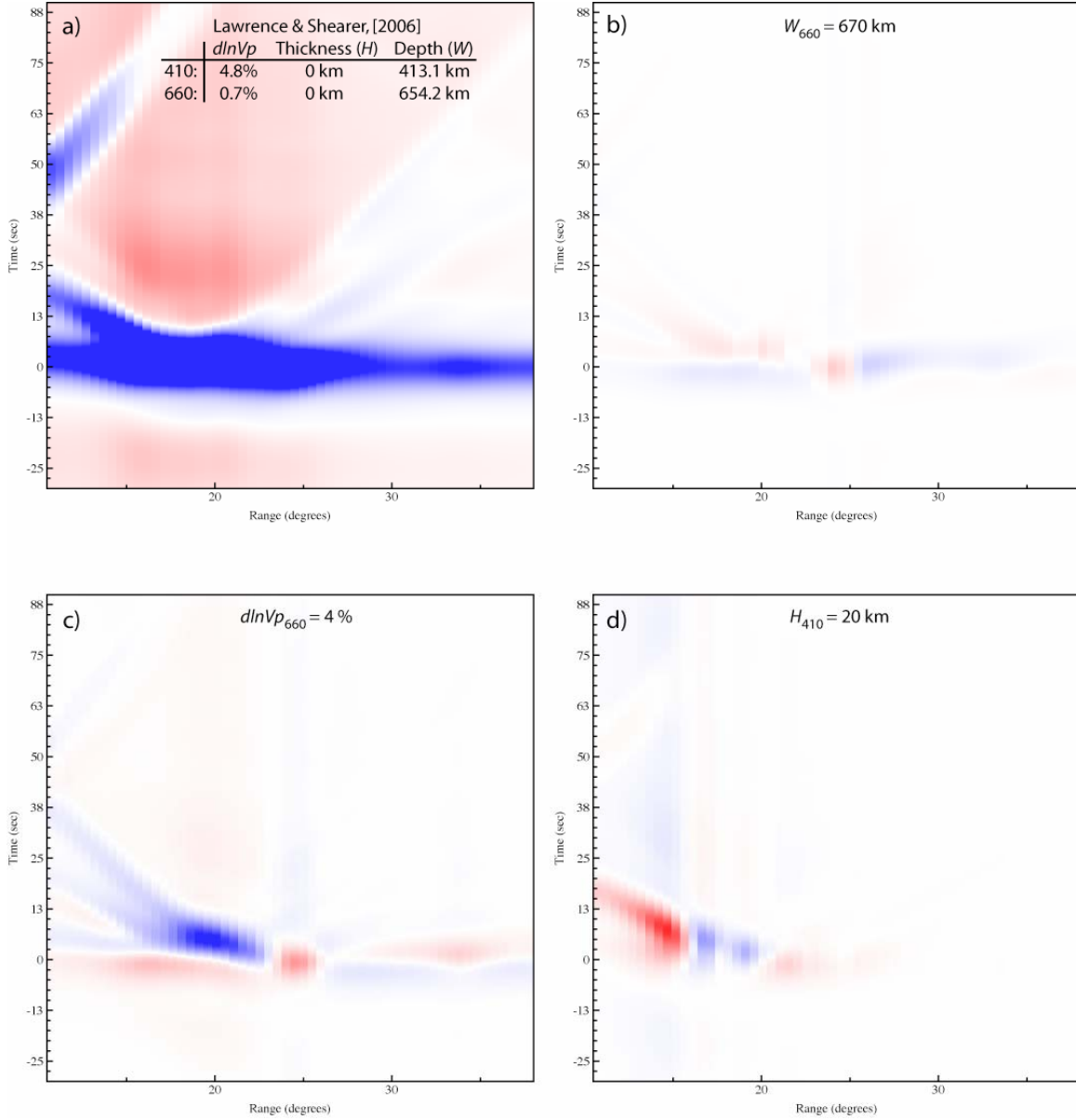


Figure 11. This figure shows (a) the synthetic Earth-response function for the seismic velocity model found by Lawrence and Shearer (2006) (LS06), and deviations in Earth-response functions relative to LS06 as a result of (b) a deeper 660 interface, (c) a larger V_{p660} contrast, and (d) a thick 410 interface. Blue is positive, red is negative.

To model these results, we calculate synthetic time- and distance-dependent Earth-response functions using WKBJ. To estimate the appropriate frequency content and heterogeneity, we deconvolve the P -wave slant-stacked synthetic waveforms from 45 to 80 degrees and convolve the stacked observed waveforms for the same distance range. Synthetics using the model of Lawrence and Shearer, (2006) (LS06) are similar, but not identical to the observed Earth-response functions (Figure 11.a). Variants from LS06 demonstrate how the Earth-response function changes as a result of structure (Figure 11.b-d).

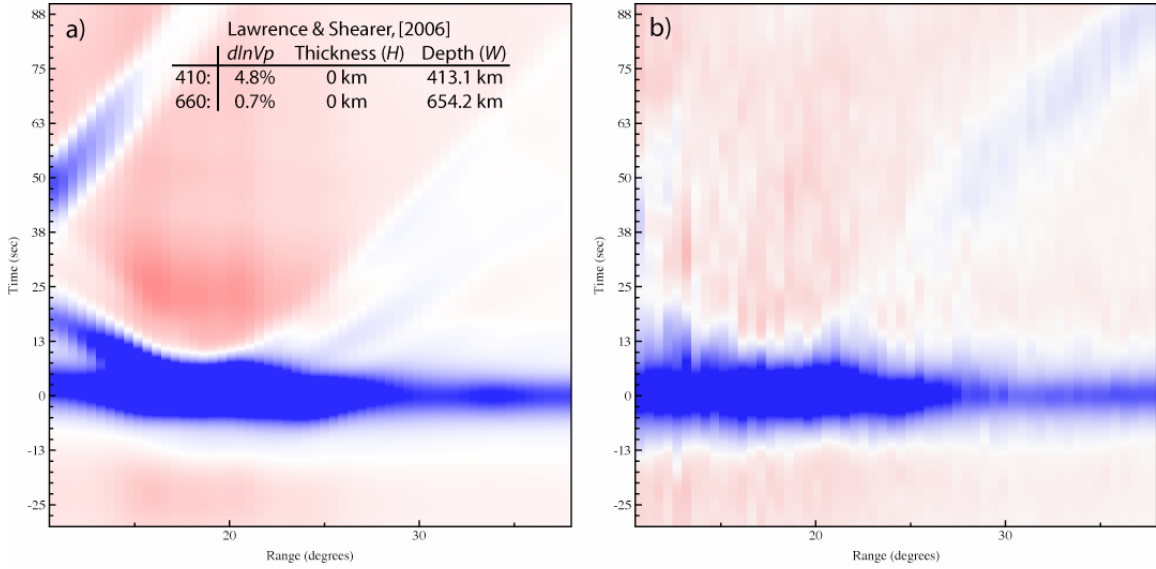


Figure 12: A comparison showing that the Earth-response function calculated from the model of Lawrence and Shearer, (2006) is very similar to the global Earth response function. These figures were calculated with decomposition using spectral division.

As shown in Figure 12, the optimal P -wave model found with a niching genetic algorithm simulated inversion for the wavefield is remarkably similar to the most optimal model found in Figure 7. Note that the most optimal model is merely representative as we assume that 3D heterogeneity has a broadening effect, and that we do not know precisely the scale of this heterogeneity. The primary difference between the optimal model found with wavefield analysis and that from amplitude analysis is that the estimated depths for the global model are slightly different, which accounts for the timing. Recall that timing is inherently included in the wavefield analysis and not in the amplitude analysis. We expect that this method will also work with shear waves, although so far we have only examined P waves.

Event Characterization

Once the station terms are well defined with the global analysis, it is possible to perform regional amplitude or wavefield analysis for high-quality individual events or sets of events. With less data it is critical to use only high-quality events and well-calibrated stations.

By deconvolving the Earth response term and station response term from the envelopes of data from a single event, it is possible to determine the magnitude based on scaling to the observed event terms (Figure 13). By scaling the global Earth response term's zero-time amplitudes to the observed zero-time amplitudes, it may be possible to estimate the event magnitude using distances between the 13 to 33 degree distance range.

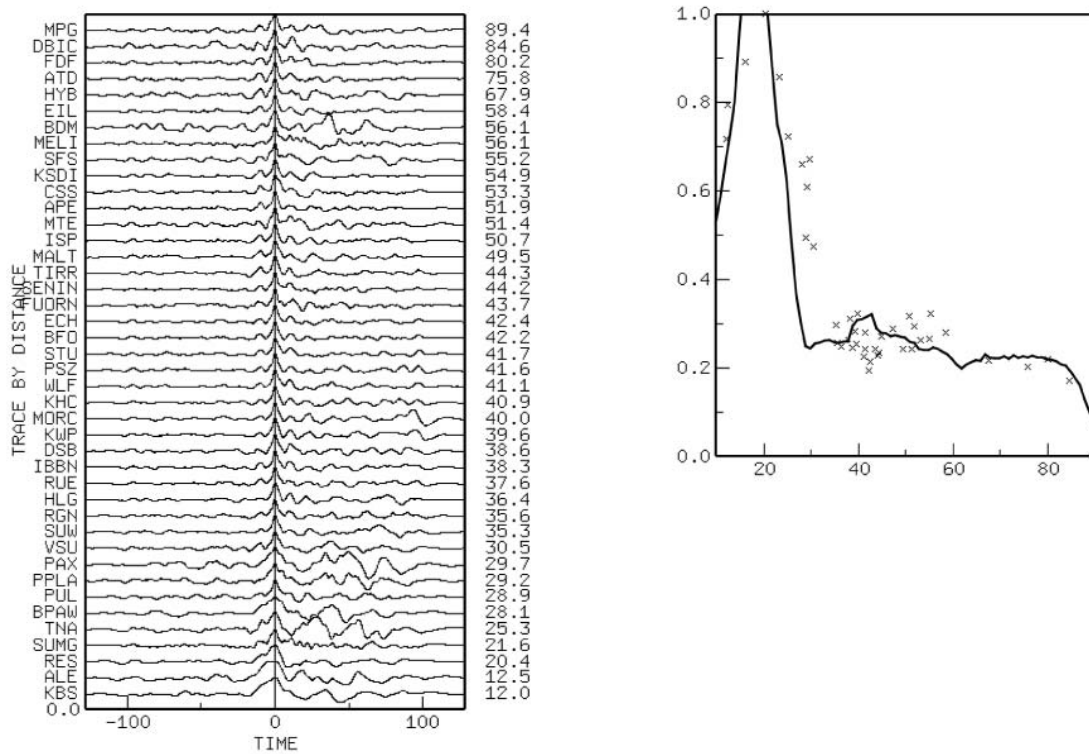


Figure 13: The Earth response term for a single event, as (left) traces, and (right) as the zero-time amplitude (x's) as a function of event-to-station distance

The scaling factors provide an estimate of earthquake magnitude. The scaling factor (sf) is correlated with body wave magnitude (M_b) with an R^2 value of 0.7 for 9 of the 12 tested events in 2005 as shown in Figure 14. Because the Earth-response term is calculated with events from 1990 to 2004, the agreement between M_b and sf is not a result of pre-constrained relations for these events. M_b and sf are related with the equation of $sf = 1.28M_b - 8.2$. Note that the results of 3 events failed due to lack of agreement (correlation) between the event and global Earth-response functions. These failures stemmed from more complex sources. The 9 more impulsive sources provided reasonable correlations between the new Earth-response term and the global Earth response term.

By using regional Earth-response functions the event magnitude estimation may become more accurate. The regional Earth-response terms will likely be more representative of regional structure and include less damping/broadening effects due to heterogeneity.

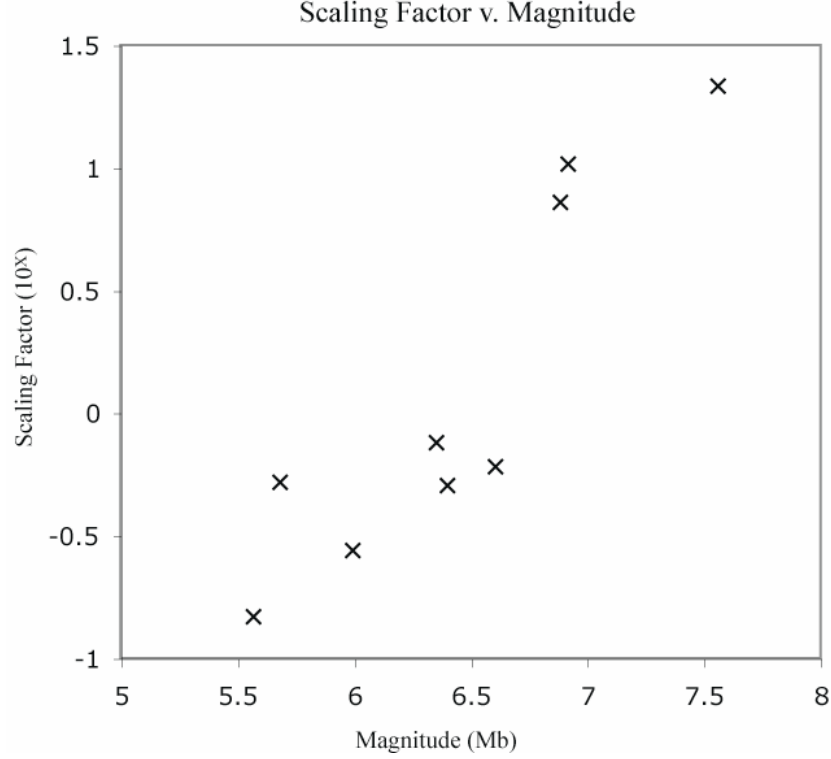


Figure 14: The relative scaling factor between the zero-time Earth-response amplitudes of a single event and the zero-time Earth-response amplitudes of the global dataset plotted versus body wave magnitude.

4. CONCLUSIONS

This analysis has shown that it is possible to divide amplitude terms from digital seismic records into source, receiver, and Earth-response terms that account for the complicated wavefield variations in the 13° and 33° distance range. Through a multi-dimensional component analysis, each term is obtained iteratively. With well-resolved receiver terms and Earth-structure, it may be possible to estimate source functions with data at these regional distances. Note that the method requires large numbers of seismograms from many stations to achieve reliable results. It is only in the past few years that global data and station coverage have increased to a sufficient level that such an analysis can be roughly conducted. In the future, improved results are likely as more data are collected from regions of increased station coverage.

By using *a priori* constraints on the Earth-response term and station terms from prior event databases, it is possible to determine the rough magnitude of some new events using the 13-33 degree distance amplitudes. This method does not work well for all new events because of complex sources, but works well for more impulsive sources.

REFERENCES

- Chambers, K., A. Deuss and J.H. Woodhouse (2005). Reflectivity of the 410-km discontinuity from PP and SS precursors, *J. Geophys. Res.*, **110**, B02301, doi:10.1029/2004JB003345.
- Chapman, C. H., (1978) A new method for computing synthetic seismograms, *Geophys. J. Astro. Soc.*, 54, 481-518.
- Flanagan, M.P. and P.M. Shearer (1998a). Global mapping of topography on transition zone velocity discontinuities by stacking SS precursors, *J. Geophys. Res.*, **102**, 2673-2692.
- Flanagan, M.P. and P.M. Shearer (1998b). Topography on the 410-km seismic velocity discontinuity near subduction zones from stacking of sS, sP, and pP precursors, *J. Geophys. Res.*, **103**, 21,165-21,182.
- Gu, Y., A.M. Dziewonski and C.B. Agee (1998). Global decorrelation of the topography of transition zone discontinuities, *Earth Planet. Sci. Lett.*, **157**, 57-76.
- Koper, D. K., M. E. Wyssession, and D. A. Wiens (1999). Multimodal function optimization with a niching genetic algorithm: a seismological example, *Bull. Seism. Soc. Am.* **89**, 978-988.
- Lawrence, J.F., and P.M. Shearer (2006) Constraining seismic velocity and density for the mantle transition zone with reflected and transmitted waveforms, G^3 , doi:10.1029/2006/GC001339.
- Masters G., G. Laske, H. Bolton, and A. Dziewonski (2000). The relative behavior of shear velocity, bulk sound speed, and compressional velocity in the mantle: implications for chemical and thermal structure, in *Earth's Deep Interior: Mineral Physics and Tomography from the Atomic to the Global Scale*, AGU Geophysical Monograph 117, AGU, Washington D.C.
- Melbourne, T. and D. Helmberger (1998). Fine structure of the 410-km discontinuity, *J. Geophys. Res.*, **103**, 10,091-10,102.
- Shearer, P.M. (1990). Seismic imaging of upper-mantle structure with new evidence for a 520-km discontinuity, *Nature*, **344**, 121-126.
- Shearer, P.M. (1991). Constraints on upper-mantle discontinuities from observations of long-period reflected and converted phases, *J. Geophys. Res.*, **96**, 18147-18182.
- Shearer, P.M. (1993). Global mapping of upper mantle reflectors from long-period SS precursors, *Geophys. J. Int.*, **115**, 878-904.

- Shearer, P.M. (2000). Upper mantle seismic discontinuities, in *Earth's Deep Interior: Mineral Physics and Tomography from the Atomic to the Global Scale*, AGU Geophysical Monograph 117, 115-131.
- Shearer, P.M. and M.P. Flanagan (1999). Seismic velocity and density jumps across the 410- and 660-kilometer discontinuities, *Science*, **285**, 1545-1548.
- Shearer, P.M. and T.G. Masters (1992). Global mapping of topography on the 660 km discontinuity, *Nature*, **355**, 791-796.
- Veith, K.F. and G.E. Clawson (1972). Magnitude from short-period P-wave data, *Bull. Seismol. Soc. Am.*, **62**, 435-452.

List of Symbols, Abbreviations, and Acronyms

DMC	Data Management Center
FARM	Fast Archive Recovery Method
IRIS	Incorporated Research Institutions in Seismology
NGA	Niching Genetic Algorithm
PASSCAL	Program for the Array Studies of the Continental Lithosphere
RAID	Redundant Array of Inexpensive Disks
SAC	Seismic Analysis Code
WKBJ	Wentzel-Kramers-Brillouin-Jeffreys